



A new perspective for effect of Bi on the photocatalytic activity of Bi-doped TiO₂

Yin Hu, Yuantao Cao, Peixian Wang, Danzhen Li*, Wei Chen, Yunhui He, Xianzhi Fu, Yu Shao, Yi Zheng

Research Institute of Photocatalysis, National Research Center of Environmental Photocatalysis, Fujian Provincial Key Laboratory of Photocatalysis-State Key Laboratory Breeding Base, Fuzhou University, Fuzhou 350002, PR China

ARTICLE INFO

Article history:

Received 19 February 2012

Received in revised form 20 May 2012

Accepted 27 May 2012

Available online 5 June 2012

Keywords:

Bi-doped TiO₂

Amorphous

Visible light

Photocatalysis

Benzene

ABSTRACT

In the current work, a simple approach, directly mixing Bi₂O₃ powder with TiO₂ sol, was developed to fabricate Bi-doped TiO₂ photocatalyst. The obtained product was characterized by powder X-ray diffraction (XRD), transmission electron microscopy (TEM), Raman spectra analysis, X-ray photoelectron spectra (XPS) and UV-vis diffuse reflectance spectroscopy (DRS). On the basis of the above characterization results, it was found that the excess Bi₂O₃ loading (>5 mol%) and sol-gel processing route could lead to the formation of Bi_xTiO_y. The XRD data pointed out that Bi_xTiO_y remained amorphous up to 500 °C and crystallized into the distinctive phase Bi₂Ti₄O₁₁ at higher temperature of 700 °C. It was worth mentioning that the participation of the distinctive microstructures made the finishing point of the doped photocatalyst, that is, strong spectral response in visible region and marked activity during the photooxidation of gaseous benzene under visible light illumination ($\lambda > 450$ nm). Furthermore, the calcination temperature also had an important effect on the photocatalytic activity. The optimal dosage of 10 mol% Bi in TiO₂ and sintering temperature of 400 °C achieved the best photocatalytic activity. Finally, the amorphous Bi_xTiO_y microstructures formed in TiO₂ crystal made a significant contribution in providing large specific surface area and more activated units regarding the photocatalytic process. It is hoped that our current work will contribute to a better understanding of the existence form of bismuth in TiO₂ crystal. More generally, it suggests the incorporation of bismuth into a simple oxide of wide band gap as a strategy to design photocatalysts with excellent properties.

© 2012 Elsevier B.V. All rights reserved.

1. Introduction

Faced with the significant environmental problems, extensive research on the elimination of hazardous chemical compounds has been developed in the past several decades. Photocatalytic oxidation using semiconductors, as an emerging advanced oxidizing technology, is now attracting more and more attention of a large number of scholars [1]. To date, TiO₂ is still the leading photocatalyst because it can mineralize a large range of organic pollutants [2–6]. Compared with other semiconductors, TiO₂'s great advantages lie in the fact that it possesses appropriate flat band potential and high chemical stability. However, its further practical application is limited for several reasons. Firstly, due to its large band gap energy (typically <380 nm), TiO₂ can only absorb ultraviolet light rather than visible light that occupies the great part of solar light. Secondly, the overall quantum yield rate can be influenced by the low rate of electron transfer to dissolved oxygen and a high rate of recombination between electron–hole pairs [7]. To solve these problems, numerous efforts have been attempted to modify the bulk electronic properties of TiO₂ photocatalysts, such

as the aggradation of noble metals [8], organic dye sensitization [9], coupling with other semiconductors [10–13] and introduction of either anions (such as N^{3–}, S^{2–} or C^{4–}) [14–17] or cations (like V⁵⁺, Fe³⁺) [18]. In addition, a variety of novel visible light responsive photocatalysts with high activity have been successfully developed [19–22]. Coupling of TiO₂ with other narrow band gap semiconductors are proved to be an important strategy for extending the light absorption spectra to the visible region and improving the photocatalytic efficiency. It is worth noting that the photocatalytic efficiency is closely related to the concentration of the dopants, preparation methods and post-treatment process. Bismuth oxide (Bi₂O₃), as a promising semiconductor to be coupled with TiO₂, is an attractive material for the photooxidation of pollutants because of its direct band gap of 2.8 eV and diversity in crystal structures [23,24]. Till date, there are lots of studies about the preparation of Bi₂O₃/TiO₂ composite and Bi-doped TiO₂. It has been shown that the Bi₂O₃ coupled or bismuth-doping TiO₂ system is more effective in the case of the photodegradation of organic pollutants under visible light irradiation. However, the existence form of bismuth is still a hot debate. According to Ji et al. [25], the result of XRD analysis demonstrated that Bi cations have doped into the crystal structure of TiO₂ when the mol ratio of Bi³⁺/Ti⁴⁺ increased from 0 to 0.051. At the same time, Li et al. [26] found the same result of the doped Bi ions substitute some of the lattice

* Corresponding author. Tel.: +86 591 83779256; fax: +86 591 83779256.

E-mail address: dzli@fzu.edu.cn (D. Li).

titanium atoms and a new discovery of Bi^{3+} and Bi^{4+} ions coexist by using X-ray diffraction, UV-visible diffuse reflectance spectra, and X-ray photoelectron spectroscopy. However, Zuo and co-workers [27] pointed out that bismuth doping causes titania to react with Bi^{3+} ions to produce Bi_xTiO_y which results in band-gap narrowing, and the threshold energy for photoactivation is reduced, potentially increasing photoactivity under illumination. Xu also prepared Bi-doped TiO_2 photocatalyst and the higher photocatalytic activity of TiO_2 doped with Bi above 1 at.% can be attributed to the formation of $\text{Bi}_4\text{Ti}_3\text{O}_{12}$ phase in TiO_2 [28], whereas Mazurkovich and Kobasa [29] considered that the decrease in activity at significant Bi_2O_3 concentrations may also be due to the formation of bismuth titanates, which are known to have low catalytic activity.

As mentioned above, there is no general agreement as to the effect of Bi doping on the properties of the binary Bi_2O_3 – TiO_2 system. In this context, it is of interest to investigate the environment of bismuth in Bi_2O_3 – TiO_2 material. In the present study, a simple method had been developed to fabricate Bi-doped TiO_2 with different Bi/Ti molar ratios. The most attractive feature of this procedure was that a relatively high concentration of Bi_2O_3 was introduced into TiO_2 to understand the Bi species modification. In particular, a series of verification experiments were designed to expressly support these findings. Furthermore, the photocatalytic activities of the composites had been evaluated by the degradation of gaseous benzene under visible light irradiation. To the best of our knowledge, few works have been published on the degradation of gas-phase benzene which is extremely toxic and carcinogenic for the Bi-doped TiO_2 photocatalyst, particularly under visible light irradiation. The related possible mechanism of enhanced photocatalytic activities of Bi_2O_3 – TiO_2 system was also discussed. This work has scientific significance and gives a better understanding about the condition of the bismuth in the binary Bi_2O_3 – TiO_2 system and its role in the photocatalytic activity.

2. Experimental

2.1. Catalyst preparation

All reagents were of analytical grade and used without further purification. Prior to the preparation of Bi-doped TiO_2 samples, pure Bi_2O_3 was prepared first. 0.01 mol of $\text{Bi}(\text{NO}_3)_3 \cdot 5\text{H}_2\text{O}$ was dissolved with 100 mL of distilled water in a conical flask with constant agitation. When a white suspension was obtained, 10 mL of 4 M NaOH aqueous solution was added till the pH value was 12. After continuous stirring for 12 h, the color of the suspension changed from white to yellow. Finally, the yellowish precipitate was centrifuged and washed with distilled water and absolute ethanol for several times, and then dried at 60 °C in a vacuum drier to obtain the final faint yellow Bi_2O_3 powder. The TiO_2 colloidal solution was synthesized using $\text{Ti}(\text{OC}_3\text{H}_7)_4$ as the precursor. 1.3 mL of HNO_3 , 180 mL of H_2O and 15 mL of $\text{Ti}(\text{OC}_3\text{H}_7)_4$ were respectively added into a conical flask and stirred continuously at 40 °C for 24 h to form a highly dispersed TiO_2 colloidal solution. Then the as-prepared Bi_2O_3 powder was equably dispersed in self-made TiO_2 colloid with sustained stirring for 12 h, and the mixture was ultrasonically dispersed for 0.5 h and dried using a microwave oven. Finally, these samples were calcined at different temperatures for 3 h and cooled down to room temperature. By changing the amount of the added Bi_2O_3 powder, the Bi-doped TiO_2 samples with different Bi/Ti molar ratios were synthesized. The resultant products were labeled by $x\%$ BT, where $x\%$ refers to the Bi/Ti molar ratio. At the same time, self-made pure TiO_2 was used as a reference compound. The heating method of TiO_2 was the same as the treatment of Bi-doped TiO_2 samples. The resultant xerogel was heated at certain temperature for 3 h and the target products were obtained. Upon calcination at 400 °C, the

pure TiO_2 was formed and designated as T400. N-doped TiO_2 was also prepared by calcination at 400 °C for 3 h under dry NH_3 flow which was expressed as NTH400. In addition, commercial $\text{Bi}_2\text{Ti}_4\text{O}_{11}$ (com-Bi₂Ti₄O₁₁) was additionally purchased from Alfa Aesar.

2.2. Catalyst characterization

The crystal structures of the prepared catalysts were determined by using a Bruker D8 Advance X-ray diffractometer at 40 kV and 40 mA with Ni-filtered $\text{Cu K}\alpha$ radiation. The transmission electron microscope (TEM) and high-resolution transmission electron microscope (HRTEM) were recorded on a FEI Tecnai G2 F20 instrument operated at an accelerating voltage of 200 kV. Laser Raman spectra were recorded on Renishaw inVia Raman systems at room temperature and equipped with the 514 nm line of an Ar ion laser as an excitation source. Nitrogen adsorption/desorption isotherms were measured at 77 K using a Micrometrics ASAP 2020 system and the Brunauer–Emmett–Teller (BET) method was applied to calculate the specific surface area and pore volume of the samples. A Varian Cary 500 UV-vis spectrophotometer was used to investigate the light absorption properties of the samples and BaSO_4 was used as a reflectance standard. X-ray photoelectron spectroscopy (XPS) spectra were acquired using an ESCALAB 250 photoelectron spectrometer (Thermo Fisher Scientific) at 3.0×10^{-10} mbar with monochromatic $\text{Al K}\alpha$ radiation ($E = 1486.2$ eV). The photoelectrochemical experiment was performed using a CHI-660D electrochemical workstation (CH Instruments, USA) in a conventional three-electrode electrochemical cell, filled with 0.1 M of Na_2SO_4 electrolyte (30 mL). A Pt plate was used as the counter electrode, and an $\text{Ag}/\text{AgCl}/\text{sat. KCl}$ electrode was used as the reference electrode. Bi_2O_3 , TiO_2 and Bi-doped TiO_2 samples were deposited as a film form on a 5 mm × 5 mm ITO conductive glass that served as the working electrode. Electron paramagnetic resonance (EPR) was used to detect radicals spin-trapped by 5,5-dimethyl-l-pyrroline N-oxide (DMPO). The signals were collected by a Bruker model A300 spectrometer (Bruker Instruments, Inc.) with the settings of center field (3512.48 G), microwave frequency (9.86 GHz), and power (6.35 mW). The light source was a 500 W Xe-arc lamp equipped with an IR-cutoff filter ($\lambda < 900$ nm) and an UV-cutoff filter ($\lambda > 450$ nm).

2.3. Measurement of photocatalytic activity

Catalysts were packed into a fixed-bed quartz reactor (4 cm × 3 cm × 0.1 cm) and the measurement of photocatalytic activity was operated in a continuous-flow mode at ambient conditions. To keep the conformity of each photocatalytic test, all samples were passed through a stainless steel sieve to obtain a mean particle size of 0.21–0.25 mm and the weight was kept constant at 1.35 g. Benzene fixed at a certain concentration (about 160 ppm) was immersed in an ice-water bath and supplied by bubbling with pure oxygen from a gas cylinder at a total flow rate of $20 \text{ cm}^3 \text{ min}^{-1}$. The reactor was irradiated by a 500 W Xe-arc lamp equipped with an IR-cutoff filter ($\lambda < 900$ nm) which was placed at a fixed distance. Meanwhile, an UV-cutoff filter ($\lambda > 450$ nm) was used as visible light source and a band pass filter that permitted only UV light was employed as the UV-light source (280 nm < λ < 400 nm). The real-time detection of benzene and carbon dioxide was conducted by an online gas chromatograph (HP6890) system which was equipped with a flame ionization detector (FID), a thermal conductivity detector (TCD), and a Porapak R column. Before an activity measurement, benzene was thermally stable without illumination and the adsorption–desorption equilibrium of benzene gas on sample was obtained after 12 h in dark. As a comparison, the degradation of benzene on self-made T400,

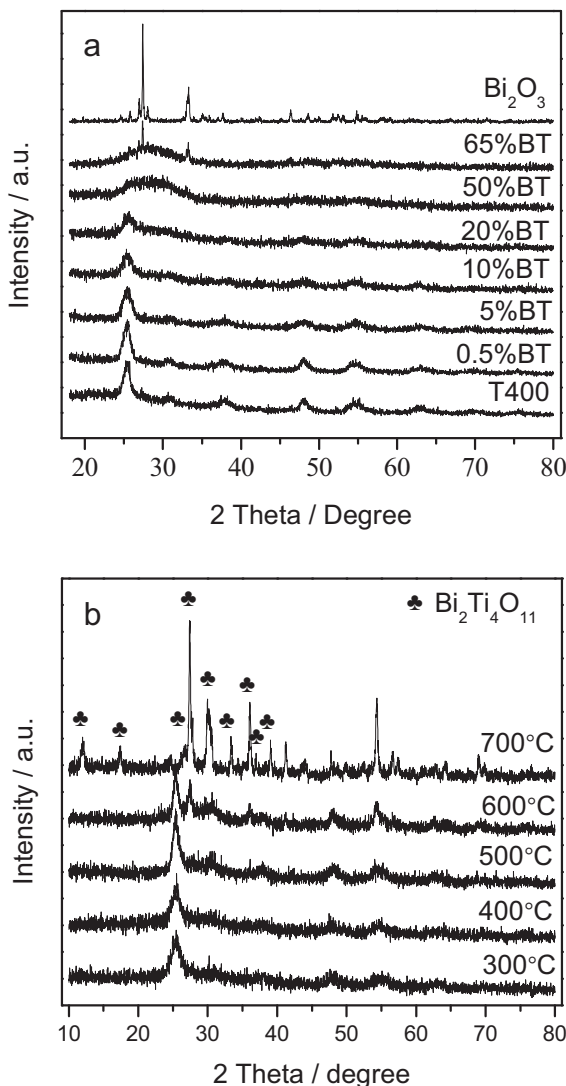


Fig. 1. XRD patterns of Bi_2O_3 , T400 and Bi-doped TiO_2 with different Bi/Ti molar ratios calcined at 400 °C (a) and 10% BT calcined at different temperatures (b).

commercial TiO_2 (P25, Degussa Co.) and NTH400 was also tested under the same conditions with an equal amount of catalyst loaded.

3. Results

3.1. XRD analysis

Fig. 1a shows the XRD patterns of the Bi-doped TiO_2 with different Bi/Ti molar ratios after calcination at 400 °C for 3 h. For comparison, the XRD patterns of the as-prepared pure Bi_2O_3 and T400 particles were also presented. As it can be seen in Fig. 1a, the XRD pattern of the as-prepared Bi_2O_3 was corresponding to the monoclinic phase of $\alpha\text{-Bi}_2\text{O}_3$ (JCPDS No. 41-1449), while the T400 was corresponding to the anatase phase of TiO_2 (JCPDS No. 21-1272) with a small amount of brookite detected. No significant diffractional peak belonging to Bi_2O_3 phase was observed until the doping concentration was up to 65%. With the increasing of Bi/Ti molar ratio from 0.5% to 65%, the anatase phase peaks gradually weakened and then disappeared. When the molar ratio of Bi/Ti was 65%, the peaks corresponding to monoclinic Bi_2O_3 appeared. From Fig. 1b, when the 10% BT sample was calcined under higher temperature (>500 °C), a new phase assigned to $\text{Bi}_2\text{Ti}_4\text{O}_{11}$ phase was observed (JCPDS No. 15-0325). It is consistent with the XRD pattern

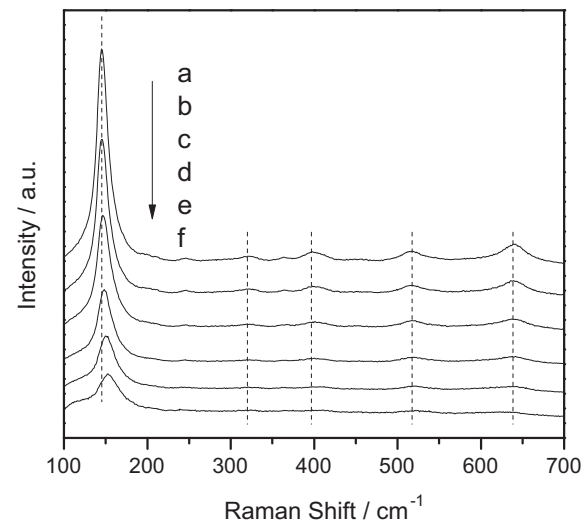


Fig. 2. Raman spectra of Bi-doped TiO_2 with different molar ratios calcined at 400 °C for 3 h: (a) T400; (b) 0.5%; (c) 5%; (d) 10%; (e) 20%; (f) 50%.

of com- $\text{Bi}_2\text{Ti}_4\text{O}_{11}$ (Supplementary Data, Fig. S1). Almost all Bi_2O_3 were converted to the $\text{Bi}_2\text{Ti}_4\text{O}_{11}$ phase when catalysts were calcined at temperature higher than 700 °C. Actually, when the molar ratio of Bi/Ti was above 5%, the phase began to appear and had a good crystallization at a higher temperature (Fig. S2).

3.2. Raman analysis

Fig. 2 presents the Raman spectra of Bi-doped TiO_2 with different Bi/Ti molar ratios calcined at 400 °C for 3 h. For comparison, the Raman spectrum of T400 is also shown in the same figure. The major peaks at 144, 319, 399, 519 and 639 cm^{-1} can be attributed to the characteristic bands of anatase phase TiO_2 , indicating that the anatase TiO_2 was the dominant phase structure [30]. With the increase of Bi loading, the intensity of the bands decreased gradually. Particularly, comparing the highest frequency peak at 144 cm^{-1} of different samples, it can be evidently seen that the intensities of this peak were weaker and peak widths were broadened compared with the T400 after bismuth doping. This indicates that the crystallinity became poor, which was consistent with the results of the XRD measurement. More importantly, as the doping level increased up to 50%, the sample had a shift by 7.1 cm^{-1} . And for the 10% BT sample, the peak also had a positive shift from 144.34 cm^{-1} to 149.14 cm^{-1} . The Raman spectra of 65% BT and pure Bi_2O_3 are also given (Fig. S3). The Raman bands of pure Bi_2O_3 were assigned to the monoclinic Bi_2O_3 phase bonds (Raman peaks at 103, 119, 140, 152, 185, 211, 282, 315, 412, 448 and 530 cm^{-1}). When the Bi doping concentration was 65%, the peaks corresponding to the monoclinic Bi_2O_3 appeared because there was an excess of Bi in the composition at this moment. And that, the Raman spectra, also corroborate well with the XRD results.

3.3. Morphology measurement

The morphology of the as-synthesized 10% BT samples is demonstrated in Fig. 3. The low-magnification TEM image (Fig. 3a) showed that the composite was composed of mutually aggregated nanoparticles, and the high-magnification TEM image (HRTEM, Fig. 3b) showed that these nanoparticles huddled together had an average size of 8–10 nm. It was clear that the observed lattice spacing of 0.352 nm and 0.238 nm corresponded to the (101) and (004) crystal planes of the anatase TiO_2 , respectively. No other crystalline phase, such as $\text{Bi}_2\text{Ti}_4\text{O}_{11}$, was observed from the HRTEM image.

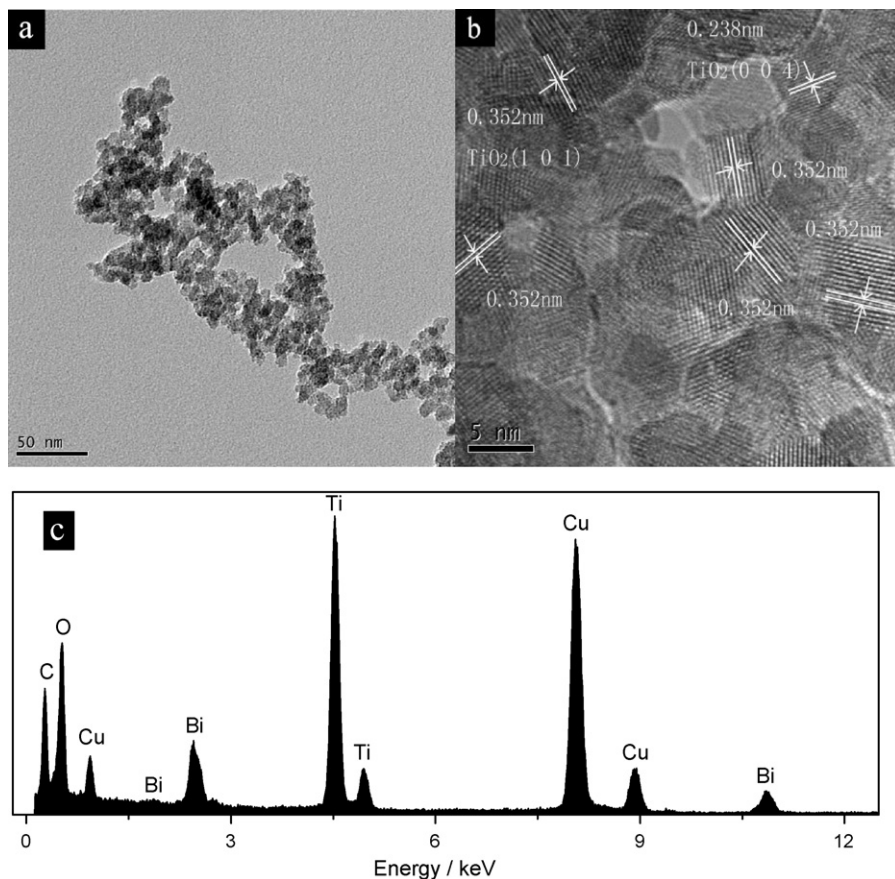


Fig. 3. Representative TEM and HRTEM images of 10% BT calcined at 400 °C (a, b) and EDS spectrum (c) of the nanoparticles in b.

Energy-dispersive X-ray spectroscopy (EDS) was applied to detect the composition of the sample. As it can be seen from Fig. 3c, five different kinds of elements were marked. The elements Cu and C were from copper grid, while the appearance of the other elements Ti, Bi, O showed that the Bi-doped TiO₂ photocatalyst indeed contain TiO₂ and bismuth-based compound. It shows that the 10% BT sample contains TiO₂ and bismuth-based compound. In addition, the TEM images of other samples are also given in Fig. S4. As shown in Fig. S4a, the as-synthesized 0.5% BT sample was composed of large of nanoparticles with size in the range of 8–10 nm, which was similar to the 10% BT sample. Actually, the only difference was that more nanoparticles in 10% BT gathered. But when the 10% BT sample was treated at 700 °C, the situation was completely different (see Fig. S4c). We have found that the particles became bigger with the size of 50–80 nm, and the reason may due to the high temperature treatment in the preparation. A representative HRTEM image with clear lattice fringes is shown in Fig. S4d. The observed lattice spacing of 0.75 nm and 0.32 nm corresponded to the Bi₂Ti₄O₁₁ phase.

3.4. XPS analysis

Fig. 4 shows the further characterization of Bi species presented in Bi-doped TiO₂ by XPS. The binding energy (BE) scales of all samples were calibrated with respect to the C 1s photoemission (284.6 eV). Clearly, it can be seen that the Bi 4f and Ti 2p photoelectron peaks of Bi-doped TiO₂ were slightly different with pure samples. The Bi 4f_{7/2} and Bi 4f_{5/2} levels for pure Bi₂O₃ were located at binding energies of 159.2 eV and 164.5 eV, respectively, while the positions of main Bi 4f_{7/2} and Bi 4f_{5/2} peaks of com-Bi₂Ti₄O₁₁ fell in 158.6 eV and 164 eV. The BE of Bi 4f_{7/2} in the Bi-doped TiO₂

compounds, however, was shifted by –0.2 to –0.5 eV with respect to the Bi 4f_{7/2} position in the pure Bi₂O₃. The direction of this shift has a tendency to that observed for com-Bi₂Ti₄O₁₁. The Ti 2p_{3/2} BE value was 458.6 eV for the T400 sample. The photoemission of Ti 2p was sensitive to the oxidation states of the elements in the com-Bi₂Ti₄O₁₁. The Ti 2p_{3/2} position of com-Bi₂Ti₄O₁₁ also had a shift to lower BE (of up to 0.4 eV). The Ti 2p_{3/2} BE values in the Bi-doped TiO₂ compounds were slightly more positive than that of the T400 (458.6 eV). The XPS spectra of the O 1s region were also given. The O 1s region of the pure T400 was located at 529.3 eV, corresponding to the Ti–O bond in TiO₂. However, the broad O 1s region of Bi₂O₃ was observed, and also the weak O 1s peak was surveyed in the com-Bi₂Ti₄O₁₁. As the Bi loading increases, the O 1s peak was weaker and had a positive shift by 0.3 eV. From the XPS measurements we can accurately determine the charge transfer between Bi, Ti, and O elements happened after doping with Bi₂O₃.

3.5. Optical properties

The corresponding UV-vis diffuse reflectance spectra of the pure Bi₂O₃, T400 and Bi-doped TiO₂ samples are listed in Fig. 5. It can be clearly seen that the light absorption exhibited regular red-shifts upon the increasing of Bi/Ti molar ratio. And in the visible region from 420 nm to 500 nm, the absorption intensities of Bi-doped TiO₂ samples were obviously higher than that of pure T400. Thus, the Bi-doped TiO₂ photocatalyst could be excited by visible light ($\lambda > 450$ nm) and exhibit a higher photocatalytic activity.

Table 1

The BET areas of pure Bi_2O_3 , T400 and Bi-doped TiO_2 with different Bi/Ti molar ratios calcined at 400 °C.

Sample	Bi_2O_3	T400	0.5% BT	5% BT	10% BT	20% BT	50% BT	65% BT
BET area ($\text{m}^2 \text{g}^{-1}$)	1.26	112.49	136.18	155.68	165.07	140.53	64.48	59.26

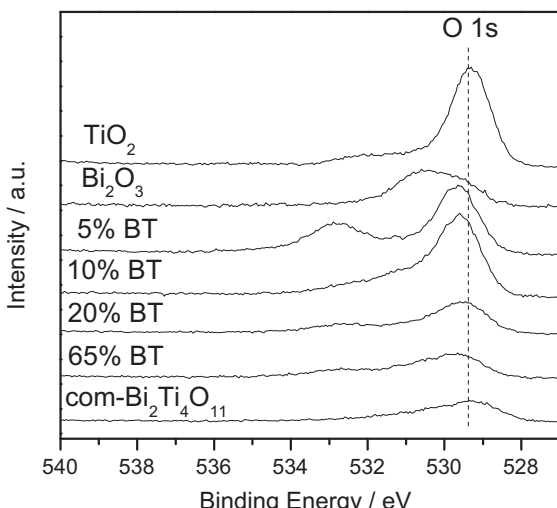
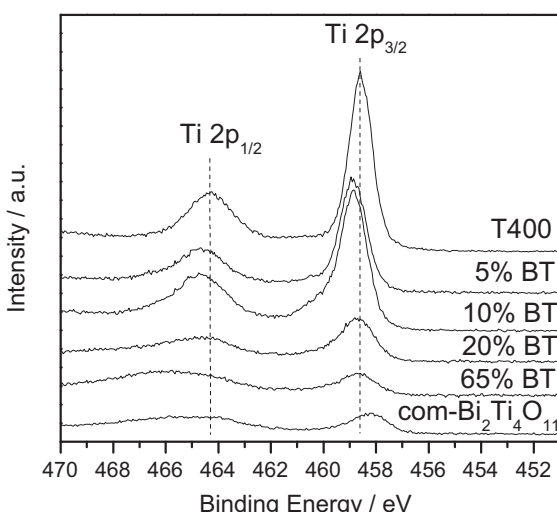
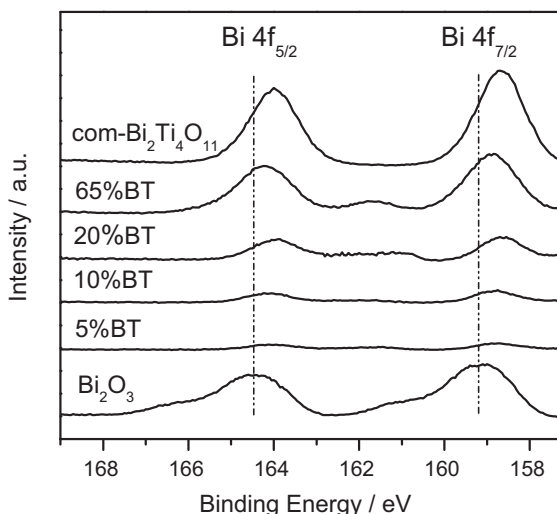


Fig. 4. XPS spectra of Bi_2O_3 , T400, com- $\text{Bi}_2\text{Ti}_4\text{O}_{11}$ and Bi-doped TiO_2 with different molar ratios calcined at 400 °C for 3 h.

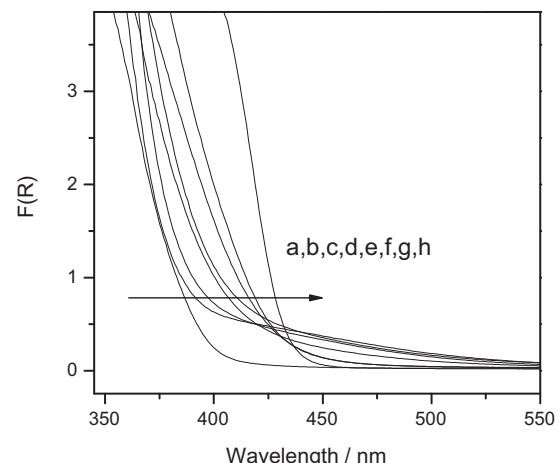


Fig. 5. DRS spectra of the samples: (a) T400; (b) 0.5% BT; (c) 5% BT; (d) 10% BT; (e) 20% BT; (f) 50% BT; (g) 65% BT; (h) Bi_2O_3 .

3.6. BET analysis

As shown in Fig. 6, the N_2 -sorption isotherm for the 10% BT sample exhibited stepwise adsorption and desorption which belonged to the type IV isotherm, indicative of a porous material. The pore size distribution plot demonstrated that the porous material had an average size distribution at 5 nm. Table 1 lists the Brunauer–Emmett–Teller specific surface areas of different catalysts calcined at 400 °C. It is obvious that the BET areas of Bi-doped TiO_2 samples appeared with regular change as the ratio of Bi/Ti increases. With the rapid increasing of Bi_2O_3 content, the BET areas increased first and then decreased. When the Bi/Ti molar ratio was 1/10, the composite possessed the biggest BET area of $165.07 \text{ m}^2 \text{ g}^{-1}$ which could be one of the significant contributions of excellent gas phase activity. The BET areas of the pure Bi_2O_3 and T400 were $1.26 \text{ m}^2 \text{ g}^{-1}$ and $112.49 \text{ m}^2 \text{ g}^{-1}$, respectively. In addition,

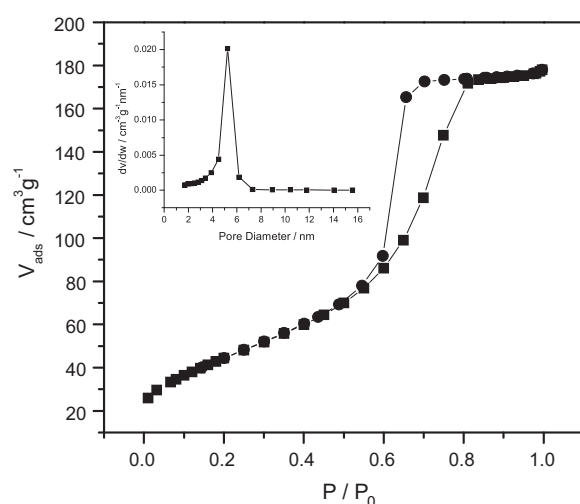


Fig. 6. N_2 adsorption–desorption isotherms of 10% BT calcined at 400 °C. The inset is pore size distribution plot. The pore size distribution was estimated from the desorption branch of the isotherm.

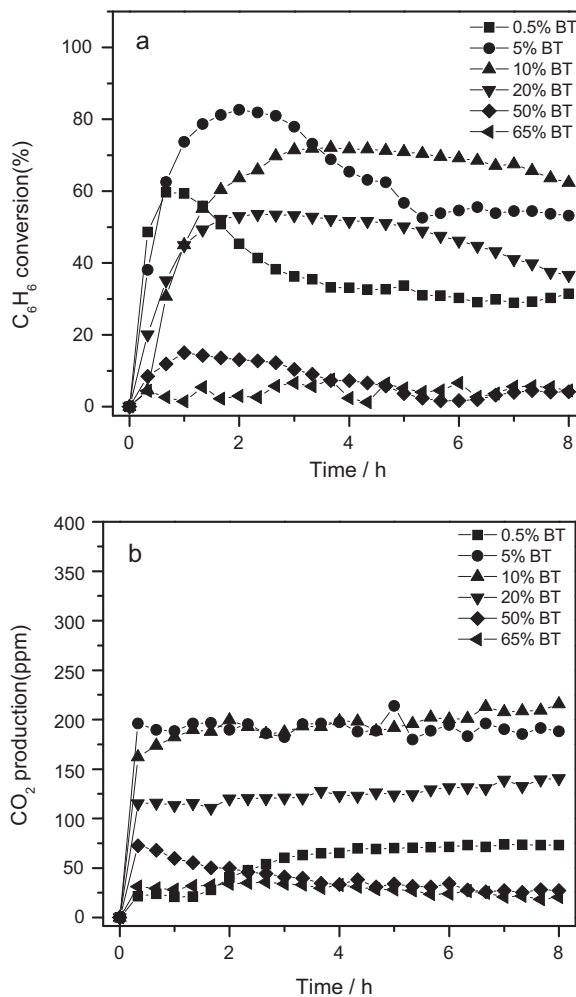


Fig. 7. (a) Conversion of C₆H₆ and (b) the amount of produced CO₂ over the Bi-doped TiO₂ samples calcined at 400 °C with different Bi/Ti molar ratios under visible light irradiation.

to understand the effect of the addition of Bi₂O₃, the BET areas of 10% BT and pure T400 calcined at different temperatures were also given (Tables S1 and S2). By contrast, we have found that the result was comparably different before and after adding Bi₂O₃. Indeed, the addition of Bi₂O₃ enlarged the BET surface areas of Bi-doped TiO₂ samples. When the treatment temperature was 400 °C, the BET area of 10% BT was 165.07 m² g⁻¹, while the pure T400 was 112.49 m² g⁻¹.

3.7. Tests of photocatalytic activity

3.7.1. The effect of Bi₂O₃ content on the photocatalytic oxidation of benzene and stability of Bi-doped TiO₂

The photocatalytic activities for benzene degradation over the as-prepared Bi-doped TiO₂ samples with different Bi/Ti molar ratios were carried out under visible light irradiation ($\lambda > 450$ nm). Fig. 7 shows the conversion of benzene and the amount of the CO₂ produced over Bi-doped TiO₂ as a function of illumination time. With the increasing Bi/Ti molar ratio, the photocatalytic activity increased first and then gradually decreased, which could fit the corresponding BET areas well. When the molar ratio of Bi/Ti was 10%, the photocatalyst presented the best photocatalytic activity toward benzene. After irradiation for first 8 h, the conversion of benzene arrived to 62.3% and more than 216 ppm CO₂ was produced after the reaction was steady, corresponding to a

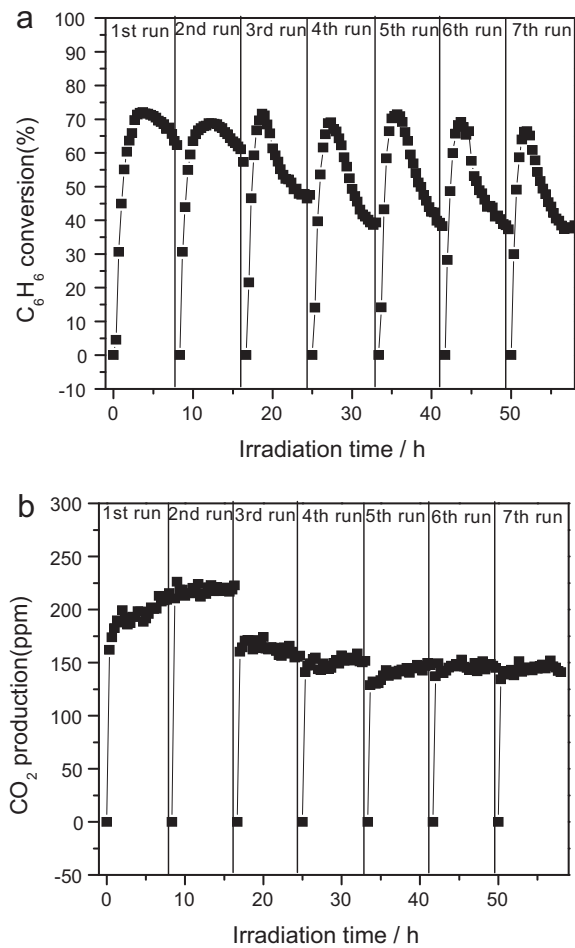


Fig. 8. Photodegradation of benzene on 10% BT photocatalyst during repetition operation upon visible light irradiation.

high mineralization ratio of about 34%. However, excessive Bi₂O₃ contents can be detrimental to the photocatalytic degradation efficiency. When the Bi/Ti molar ratio was 65%, the conversion of benzene was only 4% and only a small amount of CO₂ (ca. 20 ppm) was produced. 10% BT which performed the best activity was selected to evaluate the photocatalytic stability as shown in Fig. 8. A certain degree of deactivation was observed between the first run and third run. After that, it had begun to stabilize since the third run. From then on the conversion and the mineralization ratio could be maintained for more than 41 h. Meanwhile, the CO₂ production was initially at 216 ppm and then maintained at 147 ppm. The deactivation of 10% BT sample between the first run and third run was due to the deposition of reaction intermediates during the photocatalytic degradation of benzene which blocked the active sites on the surface of the photocatalyst [31,6,32]. The possible reaction pathways for decomposition of benzene are shown in Fig. 9. Under visible light irradiation, benzene reacted with active species to form intermediate radicals, and these intermediates could polymerize to give carbon deposits or directly decompose to CO₂ and H₂O. The formation of these organic intermediates led to the deactivation of 10% BT sample and caused the not complete mineralization of benzene. The photocatalytic degradation of benzene has proved to be complex and takes place through the formation of resistant intermediates which occupy the surface and progressively deactivate the photocatalyst [33]. According to the previous studies, phenoxy, especially phenol, was identified to be the major intermediate generated at the early stage of benzene decomposition [33–35,32,36]. In this process, the extent of

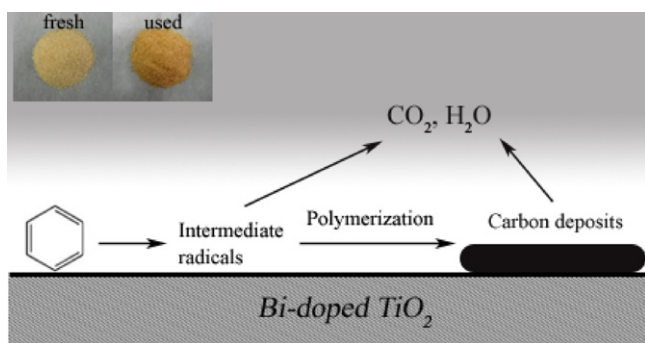


Fig. 9. Reaction pathways for photocatalytic degradation of benzene under visible light irradiation. Insert shows the colors of the fresh and used 10% BT samples.

catalyst deactivation depends on the formation and decomposition behavior of carbon deposits. After first 8 h of operation, we can see that the color of the 10% BT sample turned from pale yellow to dark yellow (as shown in the insert of Fig. 9).

3.7.2. The comparison of photocatalytic performances of different catalysts

To further understand the good photocatalytic performance of 10% BT catalyst in degrading gaseous benzene under visible light irradiation, NTH400 was chosen as a benchmarking material for comparison. As shown in Fig. 10, its efficiency of removing gaseous benzene and producing CO_2 under visible light irradiation ($\lambda > 450 \text{ nm}$) was demonstrated more than 1.95 and 1.94 times, respectively. There was a clear distinction that 10% BT was definitely superior to the P25 and pure Bi_2O_3 which had no activities toward benzene.

3.7.3. Photocatalytic activity tests under UV light irradiation

Fig. 11 shows the variation of benzene concentration and the concentration of the CO_2 produced over Bi-doped TiO_2 samples as a function of irradiation time. All samples were measured under the same conditions. When the system was illuminated with UV light, BT samples had different photocatalytic performances. Obviously, 10% BT sample presented the highest activity and the conversion of benzene reached 14%. More than 79 ppm of CO_2 produced, correspond to a high mineralization ratio of about 72%. P25, as an excellent UV-light-induced photocatalyst, was used to compare with 10% BT sample. After irradiation for first 8 h, the conversion of benzene was only 5.45% and more than 48 ppm CO_2 was produced after the reaction was steady. As shown in Fig. 12, the

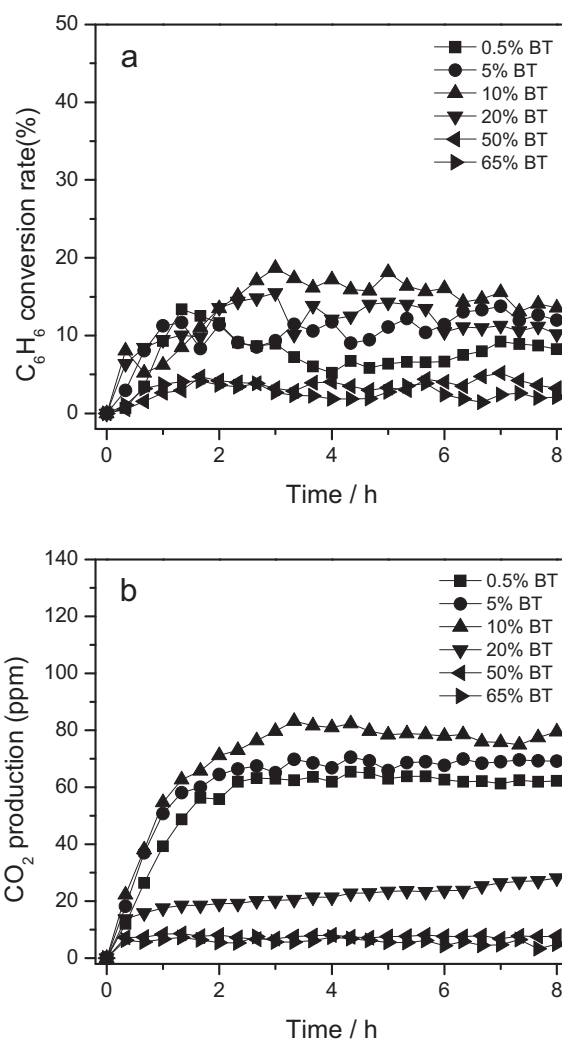


Fig. 11. (a) Conversion of C_6H_6 and (b) the amount of produced CO_2 over the Bi-doped TiO_2 samples calcined at 400°C with different Bi/Ti molar ratios under UV light irradiation.

photocatalytic activity of 10% BT was significantly higher than P25. Its efficiency of removing gaseous benzene and producing CO_2 under UV light irradiation was demonstrated more than 2.5 and 1.6 times, respectively. Therefore, the existence of Bi is also favorable to

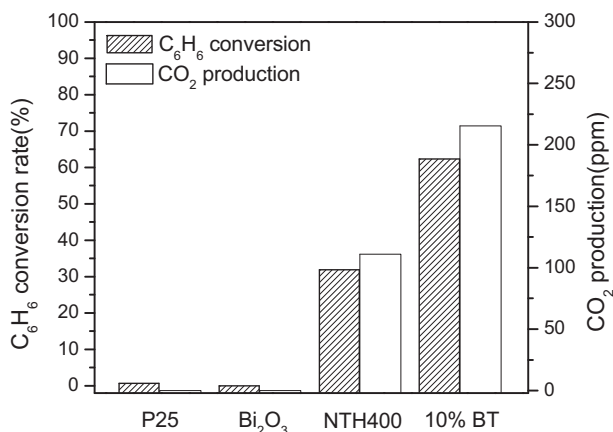


Fig. 10. Photocatalytic performances of different catalysts for decomposing benzene in air under visible light irradiation.

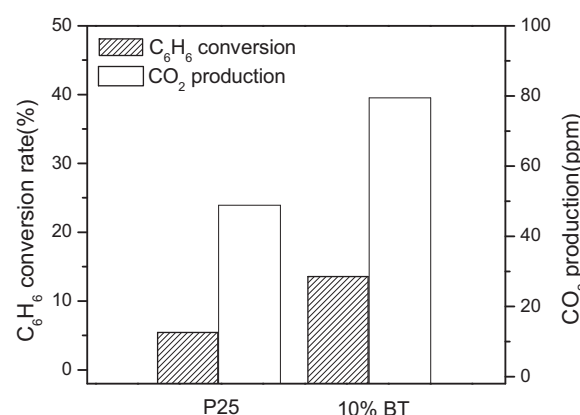


Fig. 12. Photocatalytic performances of P25 and 10% BT for decomposing benzene in air under UV light irradiation.

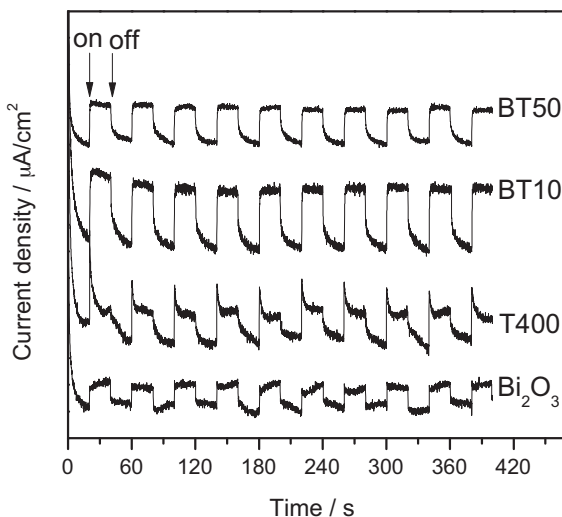


Fig. 13. Photocurrent action spectra of Bi_2O_3 , T400 and Bi-doped TiO_2 electrodes under visible light irradiation ($\lambda > 450 \text{ nm}$).

enhance the photocatalytic activity of Bi-doped TiO_2 under UV light irradiation.

3.8. Photoelectrochemistry property

To understand the good photocatalytic activity of Bi-doped TiO_2 samples better, photoelectrochemical technique was applied to study the charge transfer and recombination processes at semiconductor/electrolyte interfaces.

The photocurrent density–time ($I-t$) profiles without any bias electrode potential were given as shown in Fig. 13. The ITO/Bi₂O₃ and ITO/T400 electrodes were measured first. When the system was irradiated with visible light, the measured photocurrent showed a rapid rise, and soon increased to a steady value with instant illumination time. Then, the photocurrent rapidly fell down to the initial value as the light was turned off. During irradiation, the current was stable at given time intervals (20 s). It can be seen that there was only a subtle difference in the photocurrent between the ITO/Bi₂O₃ and ITO/T400 electrodes under visible light irradiation. The photocurrent was enhanced and more stable after doping with Bi. With the amount of Bi₂O₃ increasing, the photocurrent of the ITO/Bi-doped TiO_2 electrode decreased though it was larger than that of the ITO/Bi₂O₃ and ITO/T400 electrodes all along. The maximum photocurrent appeared at a mole ratio of 10%, which was well matched with the photocatalytic experiments.

3.9. EPR spectroscopy

As we know, the reactive oxygen species such as $\text{O}_2^{\bullet-}$ and $\cdot\text{OH}$ radicals play very important roles in the photocatalytic process. Herein, EPR spin-trap with DMPO technique [37,38] has been performed to detect the relevant active species. Fig. 14 shows the EPR spectra of the visible light irradiated catalysts/DMPO aqueous dispersions under ambient conditions. When the catalysts were BT samples, a set of signals with four characteristic peaks which were assigned to DMPO $\cdot\text{OH}$ spin adducts appeared with the intensity ratio of 1:2:2:1. Obviously, an increase markedly in intensity with the increasing of Bi loadings and reached a maximum at the mole ratio of Bi:Ti = 1:10, whereas there was no obvious signal corresponding to spin-trapped $\cdot\text{OH}$ radicals in the 65% BT and pure Bi₂O₃. It indicates that the addition of Bi₂O₃ has great effect on the generation of hydroxyl radicals which was a concern for the initial rate of photooxidation of gaseous benzene. In addition,

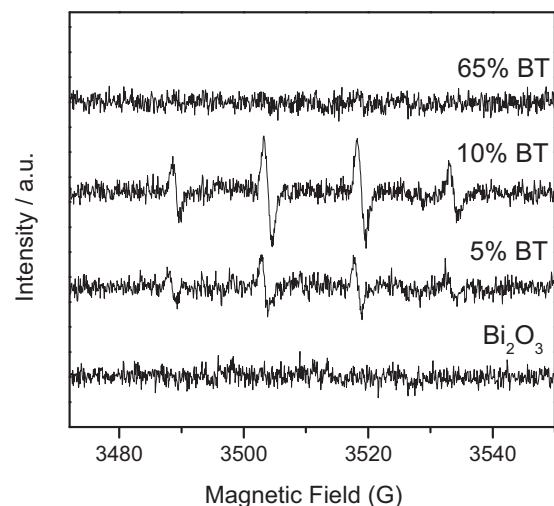


Fig. 14. EPR spectral features of the DMPO $\cdot\text{OH}$ spin adducts formed upon visible light irradiation of different photocatalysts in aqueous dispersions ($\lambda > 450 \text{ nm}$).

the EPR spectra of the BT samples in the DMPO/CH₃OH system were also investigated under visible light irradiation (Fig. S5). The six characteristic peaks, corresponding to the spin-adducts DMPO- $\text{O}_2^{\bullet-}$, could be observed in the methanol solvent. However, the intensities were extremely weak, indicating very small amount of $\text{O}_2^{\bullet-}$ being generated in catalysts/DMPO/CH₃OH system. It is reasonable to conclude that $\cdot\text{OH}$ and very small amount of $\text{O}_2^{\bullet-}$ were generated in the Bi-doped TiO_2 photocatalytic system under visible light irradiation.

4. Discussion

4.1. Characteristics of Bi-doped TiO_2

What form would the Bi exist? It seems an old question, but needs to reconsider and more will follow. Firstly, the characteristic properties could clearly construct the framework in outline. The XRD characterizations would depict the question. Doping TiO_2 with Bi shows a poor crystallinity and no Bi₂O₃ phase appears even when the dopant concentration is 50% (Fig. 1). At this time, the distinctive Bi₂Ti₄O₁₁ phase is formed when the 10% BT sample is calcinated at 700 °C for 3 h. Actually, when the molar ratio of Bi:Ti is above 5%, the phase begins to appear and has a good crystallization at a higher temperature (Fig. S2). Well, now what we should care about is that the condition at lower temperature. According to the well-studied Bi₂O₃- TiO_2 system [39–41], it is concluded that Bi₂Ti₄O₁₁ phase should remain amorphous when the calcination temperature is below 500 °C. Moreover, Bamberger pointed out that TiO_2 is not soluble in the “high-temperature” form of Bi₂Ti₄O₁₁ [42]. When the molar ratio of Bi:Ti exceeds 50%, TiO_2 is used up gradually according to the stoichiometric ratio of Bi₂Ti₄O₁₁ and the redundant Bi₂O₃ phase emerges. The present results indicate that a high sintering temperature is usually necessary for the crystallization of Bi₂Ti₄O₁₁ phase. The formation of unexpected Bi₂Ti₄O₁₁ phase is favored by an excess Bi₂O₃ powder in the composition and the sol–gel processing route. Thus, a preliminary judge is proposed, that is, Bi is in the form of amorphous Bi_xTi_y microstructures and exists independently of the TiO_2 phase. Next, more characterizations are performed. From the Raman analysis (Fig. 2), as the doping level increased up to 50 mol%, the sample has a shift by 7.1 cm⁻¹. And for the 10% BT sample, the peak also has a positive shift from 144.34 cm⁻¹ to 149.14 cm⁻¹. The peak-shift may more probably also be ascribed to oxygen stoichiometry and oxygen vacancies, caused by the formation of Bi_xTi_y [43,44]. The sol–gel and

calcination processing route are favored to the formation of Bi_xTiO_y in the binary system Bi_2O_3 – TiO_2 , although the Bi^{3+} (0.096 nm) is much bigger than Ti^{4+} (0.068 nm). Under calcination at higher temperature, the dispersed Bi-species interacts with TiO_2 to incorporate Bi-species into the TiO_2 lattice, leading to the formation of the Bi-based solid solution $\text{Bi}_2\text{Ti}_4\text{O}_{11}$ compound. At low calcination temperature, the $\text{Bi}_2\text{Ti}_4\text{O}_{11}$ phase maintains amorphous, which has poorer indicative peaks. And that, the Raman spectra, also corroborates well with the XRD results. TEM analysis can be used to examine the composition of the samples. When the 10% BT sample is treated at 700 °C, the clear lattice fringes of 0.75 nm and 0.32 nm which correspond to the $\text{Bi}_2\text{Ti}_4\text{O}_{11}$ phase are observed (Fig. S4d). But no other crystalline phase, such as $\text{Bi}_2\text{Ti}_4\text{O}_{11}$, is observed from the HRTEM image in the 10% BT sample with calcination at 400 °C (Fig. 3b). On the other hand, Bi element is also detected by EDS. It shows that the 10% BT sample indeed contains TiO_2 and bismuth-based compound. It indicates that high temperature treatment favors the crystallization of pure $\text{Bi}_2\text{Ti}_4\text{O}_{11}$. Next, the XPS analysis enriches the verification. The changes of the $\text{Ti} 2p_{3/2}$, $\text{Bi} 4f_{7/2}$ and $\text{O} 1s$ peaks clearly show that bonding and the space charges transport exist in the Bi-doped TiO_2 compounds. Thus, the bismuth doping exerts significant influence on the XPS spectra. All the results jointly determine the existing form of Bi, that is, a separate phase of amorphous Bi_xTiO_y . An excess of Bi and the calcination treatment results in the formation of the Bi_xTiO_y . As we know, the surface area of a catalyst has a great influence on the catalytic activity [45]. Thus, the increase in BET area may have a positive impact to the photocatalytic activity. From the BET results, it is quite different before and after adding Bi_2O_3 . The 10% BT sample calcined at 400 °C possesses the biggest BET area of 165.07 $\text{m}^2 \text{g}^{-1}$ (Table 1).

4.2. Influences of dopants on visible light reactivity of TiO_2

The final photocatalytic activity is susceptible to the molar ratio of Bi/Ti. The 10% BT sample which is calcined at 400 °C presents the best activity (Figs. 7 and 8). However, excessive Bi_2O_3 contents can be detrimental to the photocatalytic degradation efficiency. Thus, the facts show that the influence on the photocatalytic activity is significant in the presence of Bi_2O_3 . As mentioned above, we know that it is the amorphous Bi_xTiO_y microstructures that contribute to the good photocatalytic activity. To confirm the role of the amorphous Bi_xTiO_y , a series of extra experiments are tested from the side validation. XRD patterns of mechanical mixture of Bi_2O_3 , com- $\text{Bi}_2\text{Ti}_4\text{O}_{11}$ and T400 powders with the same molar ratio of 10% are listed in Fig. S6. From these two figures, we can find the compositions of two mixtures are exactly the combination of Bi_2O_3 , $\text{Bi}_2\text{Ti}_4\text{O}_{11}$ and anatase TiO_2 . The corresponding photocatalytic activities are also investigated as shown in Fig. S7. It is found that they could only exhibit low photocatalytic activities when the samples are mixed mechanically without calcination. As we all know, if only calcined at a high temperature, TiO_2 can strongly interact with Bi_2O_3 , which is in favor of the transfer of photogenerated carriers. Compared with the BET areas, the mechanical mixture of Bi_2O_3 , com- $\text{Bi}_2\text{Ti}_4\text{O}_{11}$ and T400 powders with molar ratio of 10% are far smaller than 10% BT (Table S3). It fully confirms the importance of calcination treatment. Furthermore, we also prepare com- $\text{Bi}_2\text{Ti}_4\text{O}_{11}$ / TiO_2 composites with different molar ratios of Bi/Ti. Heat treatment is carried out at 400 °C, in air, for 3 h. The heating up and cooling down rate for all the samples are 2 °C/min. The physical properties of the composite photocatalysts have been characterized by XRD (Fig. S8). From the XRD patterns, it can be seen that the $\text{Bi}_2\text{Ti}_4\text{O}_{11}$ phase begins to appear when the com- $\text{Bi}_2\text{Ti}_4\text{O}_{11}$ content exceeds 0.15% (molar ratio). With the increasing of com- $\text{Bi}_2\text{Ti}_4\text{O}_{11}$ loadings from 0.15% to 10%, the $\text{Bi}_2\text{Ti}_4\text{O}_{11}$ phase becomes obvious. It is shown that the photocatalysts are indeed composed of well-crystallized $\text{Bi}_2\text{Ti}_4\text{O}_{11}$ phase and anatase TiO_2 . The photocatalytic

behaviors of the composites are examined by the degradation of gaseous benzene under visible light irradiation (Fig. S9). When the molar ratio of Bi/Ti is 0.15% and 1.5%, the photocatalyst exhibits low activity for benzene degradation. The highest efficiency is observed when the molar ratio of Bi/Ti is 5%. This result further confirms that the crystallized $\text{Bi}_2\text{Ti}_4\text{O}_{11}$ / TiO_2 composites certainly have the ability in the degradation of benzene. It is just lower than 10% BT sample. The difference results from the ways of the doping behavior. The doping behavior of 10% BT sample is similar to in situ doping. Upon calcination, it can be conducted much better that Bi-dopants incorporated into TiO_2 lattice, though Bi atom is much larger than Ti atom. On the other hand, a series of Bi^{3+} -doped TiO_2 (Bi^{3+} – TiO_2) catalysts with a doping concentration up to 3 wt% are prepared in a sol–gel process [46]. Bismuth nitrate ($\text{Bi}(\text{NO}_3)_3 \cdot 5\text{H}_2\text{O}$) is used as bismuth source. The determined amount of bismuth nitrate is dissolved in TiO_2 sol under vigorous stirring to form precursor solution. The heat treatment is the same as the approach of the previous samples. The photocatalytic activities of Bi^{3+} – TiO_2 catalysts are evaluated in the photocatalytic oxidation of gaseous benzene under visible light illumination. Fig. S10 shows the XRD patterns of T400 and Bi^{3+} – TiO_2 with different Bi/Ti mass ratios calcined at 400 °C for 3 h. It can be seen that the anatase TiO_2 phase is dominant in all the samples and the intensity of the anatase TiO_2 decreases as the dopant concentration is up to 3 wt% (weight%). There are no other peaks to be detected and no additional peak shift is observed. Figs. S11 and S12 demonstrate Raman spectra and XPS spectra of Bi^{3+} -doped TiO_2 with different Bi/Ti mass ratios calcined at 400 °C for 3 h. Similarly, the major peaks at 144, 319, 399, 519 and 639 cm^{-1} can be attributed to the characteristic bands of anatase TiO_2 phase. As the Bi^{3+} increasing, the intensity of the bands decreases slightly. Most importantly, there is no any peak shift at 144 cm^{-1} observed in this figure. In addition, it can be seen that the $\text{Bi} 4f$ and $\text{Ti} 2p$ photoelectron peaks of Bi^{3+} -doped TiO_2 are almost the same as the pure Bi_2O_3 and T400 samples (Fig. S12). This confirms the fact that the Bi exists in the form of Bi^{3+} ion when the dopant concentration is relatively low, and the addition of Bi^{3+} ion does not change the crystal structure of TiO_2 . The photocatalytic degradation behaviors of the samples are illustrated in Fig. S13. The optimal doping of bismuth ion at 1 wt% is found in this study. The C_6H_6 conversion is 35%, and the corresponding CO_2 production is 129 ppm. It is proved that the Bi^{3+} ion indeed increases the photocatalytic activity, but the excess Bi ion is detrimental to the photodegradation of benzene. However, it is still lower than that of 10% BT sample. Still, all we were doing is just to illustrate a fact, that is, the formation of amorphous Bi_xTiO_y contributes to the efficient activity. The verification experiment proves that the protagonist is the amorphous Bi_xTiO_y microstructures, but not Bi^{3+} ion, Bi_2O_3 and crystallized $\text{Bi}_2\text{Ti}_4\text{O}_{11}$. Thus, together with the characterization results, we are convinced that the conclusion we proposed. The presence of oxygen vacancies in compounds of the Bi_2O_3 – TiO_2 system may play a very important role in the photocatalytic process [47,48].

The photocurrent data show that Bi-doped TiO_2 photocatalyst that adds Bi_2O_3 , subsequent to irradiation by visible light, exhibits much higher photocurrent intensity, and leads to higher degradation rate. This further confirms that a more effective charge-separation and transfer processes have occurred after TiO_2 is hybridized by excessive Bi_2O_3 . It is generally accepted that the efficiency of electron excitation, electron–hole pairs separation and charge transfer is obviously crucial to the photocatalysis system [49,50]. As shown in Fig. 14, $\cdot\text{OH}$ radicals are found to be the principal oxidizing species in the mineralization of gaseous benzene. The 10% BT sample which presents the best activity yields the most $\cdot\text{OH}$ radicals. Further increase of the Bi concentration results in poor crystallinity and smaller BET surface areas which follows less $\cdot\text{OH}$ radicals yielding. Therefore, a significant decrease of the

photocatalytic efficiency is observed at higher Bi loadings. From the above results, it seems clear that incorporation of Bi in TiO_2 can extend the spectral response to the visible region. When excessive Bi_2O_3 is loaded on the TiO_2 , the amorphous Bi_xTiO_y microstructures are formed after calcination treatment. The photocatalytic activity is improved efficiently since the existed Bi_xTiO_y species acts as electron traps and thus facilitates the charge separation. This was suggested by the previous study [43], and can also be inferred from the EPR and photocurrent results reported in this study. In summary, this approach is very conductive to reshape the understanding of Bi element behavior in the Bi-doped photocatalyst. As a result, visible light sensitization of TiO_2 by embedding Bi_2O_3 is successful and the photocatalytic activity is improved significantly.

5. Conclusion

This paper presents a new approach to prepare Bi-doped TiO_2 photocatalysts by introducing Bi_2O_3 powder into the TiO_2 colloid via a sol-gel method. During the photooxidation of gaseous benzene under visible light irradiation, the prepared catalysts exhibited higher activities than P25 and NTH400. The photocatalytic efficiency of the Bi_2O_3 – TiO_2 coupling system was highly dependent on the proportion of Bi/Ti molar ratio. It was found that the calcination temperature had an important effect on the chemical state of Bi species, which directly influenced the photocatalytic activity. More specifically, a microstructured Bi_xTiO_y forms in TiO_2 due to an excess of Bi in the composition, particularly followed by annealing treatment, contributes to the good activity. The unexpected bismuth-rich $\text{Bi}_2\text{Ti}_4\text{O}_{11}$ phase was observed by calcination above 500 °C for the first time. It was suggested that these Bi species could be preferable for bigger specific areas and improving the efficiency of the composites. The efficient photocatalytic activity may be attributed to the synergistic effect resulted from the strong combination of the microstructured Bi_xTiO_y and anatase TiO_2 . Moreover, the large BET area made the adsorbed compounds concentrated in clusters, leading to the higher photocatalytic efficiency. The simple and low cost approach would be a highly efficient means for broadening the further industrial application. This fact makes us see the hope that other visible-light-driven photocatalysts with high activity may be found by developing the simple method.

Acknowledgments

This work was financially supported by the NNSF of China (21173047, 21073036 and 21033003), National Basic Research Program of China (973 Program, 2007CB613306).

Appendix A. Supplementary data

Supplementary data associated with this article can be found, in the online version, at <http://dx.doi.org/10.1016/j.apcatb.2012.05.040>.

References

- [1] M.R. Hoffmann, S.T. Martin, W.Y. Choi, D.W. Bahnemann, Chemical Reviews 95 (1995) 69–96.
- [2] T.N. Obee, R.T. Brown, Environmental Science and Technology 29 (1995) 1223–1231.
- [3] H. Yamashita, Y. Ichihashi, M. Anpo, Journal of Physical Chemistry 100 (1996) 16041–16044.
- [4] R.M. Alberici, W.F. Jardim, Applied Catalysis B: Environmental 14 (1997) 55–68.
- [5] Z. Ding, G.Q. Lu, P.F. Greenfield, Journal of Physical Chemistry B 104 (2000) 4815–4820.
- [6] H. Einaga, S. Futamura, T. Ibusuki, Applied Catalysis B: Environmental 38 (2002) 215–225.
- [7] X.Z. Li, F.B. Li, Environmental Science and Technology 35 (2001) 2381–2387.
- [8] X.Z. Fu, W.A. Zeltner, M.A. Anderson, Applied Catalysis B: Environmental 6 (1995) 209–224.
- [9] B.O. Regan, M. Gratzel, Nature 353 (1991) 737.
- [10] X.Z. Li, F.B. Li, C.L. Yang, W.K. Ge, Journal of Photochemistry and Photobiology A: Chemistry 141 (2001) 209–217.
- [11] Y. Bessekhouad, D. Robert, J.V. Weber, Journal of Photochemistry and Photobiology A: Chemistry 163 (2004) 569–580.
- [12] Y.G. Zhang, L.L. Ma, J.L. Li, Y. Yu, Environmental Science and Technology 41 (2007) 6264–6269.
- [13] Y. Bessekhouad, D. Robert, J.V. Weber, Catalysis Today 101 (2005) 315–321.
- [14] R. Asahi, T. Morikawa, T. Ohwaki, K. Aoki, Y. Taga, Science 293 (2001) 269–271.
- [15] J.L. Gole, J.D. Stout, Journal of Physical Chemistry B 108 (2004) 1230–1240.
- [16] Y. Yu, J.C. Yu, C.Y. Chan, Y.K. Che, J.C. Zhao, L. Ding, W.K. Ge, P.K. Wong, Applied Catalysis B: Environmental 61 (2005) 1–11.
- [17] T. Ohno, M. Akiyoshi, T. Umebayashi, K. Asai, T. Mitsui, M. Matsumur, Applied Catalysis A: General 265 (2004) 115–121.
- [18] H. Yamashita, M. Harada, J. Misaka, M. Takeuchi, K. Ikeue, M. Anpo, Journal of Photochemistry and Photobiology A: Chemistry 148 (2002) 257–261.
- [19] Z.G. Zou, J.H. Ye, K. Sayama, H. Arakawa, Nature 414 (2001) 625–627.
- [20] J.W. Tang, Z.G. Zou, J.H. Ye, Angewandte Chemie International Edition 43 (2004) 4463–4466.
- [21] X.C. Wang, K. Maeda, X.F. Chen, K. Takanabe, K. Domen, Y.D. Hou, X.Z. Fu, M. Antonietti, Journal of the American Chemical Society 131 (2009) 1680–1681.
- [22] M. Sun, D.Z. Li, W.J. Li, Y.B. Chen, Z.X. Chen, Y.H. He, X.Z. Fu, Journal of Physical Chemistry C 112 (2008) 18076–18081.
- [23] L. Zhou, W.Z. Wang, H.L. Xu, S.M. Sun, M. Shang, Chemistry—A European Journal 15 (2008) 1776–1782.
- [24] L.S. Zhang, W.Z. Wang, J. Yang, Z.G. Chen, W.Q. Zhang, L. Zhou, S.W. Liu, Applied Catalysis A: General 308 (2006) 105–110.
- [25] T.H. Ji, F. Yang, Y.Y. Lv, J.Y. Zhou, J.Y. Sun, Materials Letters 63 (2009) 2044–2046.
- [26] H.Y. Li, D.J. Wang, P. Wang, H.M. Fan, T.F. Xie, Chemistry—A European Journal 15 (2009) 12521–12527.
- [27] H. Zuo, J. Sun, K. Deng, R. Su, F. Wei, D. Wang, Chemical Engineering and Technology 30 (2007) 577–582.
- [28] J.J. Xu, Y.H. Ao, D.G. Fu, C.W. Yuan, Applied Surface Science 255 (2008) 2365–2369.
- [29] Y.S. Mazurkevich, I.M. Kobasa, Inorganic Materials 38 (2002) 522–525.
- [30] T. Ohsaka, F. Izumi, Y. Fujiki, Journal of Raman Spectroscopy 7 (1978) 321–324.
- [31] O. d’Hennezel, P. Pichat, D.F. Ollis, Journal of Photochemistry and Photobiology A: Chemistry 118 (1998) 197–204.
- [32] W. Wang, Y. Ku, Journal of Photochemistry and Photobiology A: Chemistry 159 (2003) 47–59.
- [33] N. Doucet, O. Zahraa, M. Bouchy, Catalysis Today 122 (2007) 168–177.
- [34] W.C. Wu, L.F. Liao, C.F. Lien, J.L. Lin, Physical Chemistry Chemical Physics 3 (2001) 4456–4461.
- [35] W. Wang, L.W. Chiang, Y. Ku, Journal of Hazardous Materials 101 (2003) 133–146.
- [36] H.B. Yu, B.J. Kim, B.E. Rittmann, Biodegradation 12 (2001) 455–463.
- [37] C.C. Chen, P.X. Lei, H.W. Ji, W.H. Ma, J.C. Zhao, Environmental Science and Technology 38 (2004) 329.
- [38] T.X. Wu, T. Lin, J.C. Zhao, H. Hidaka, N. Serpone, Environmental Science and Technology 33 (1999) 1379.
- [39] T. Kidchob, L. Malfatti, D. Marongiu, S. Enzo, P. Innocenzi, Journal of the American Ceramic Society 93 (2010) 2897–2902.
- [40] K. Pengpat, Advances in Materials Research 55–57 (2008) 461–464.
- [41] A.I. Akimov, G.K. Savchuk, Inorganic Materials 40 (2004) 716–720.
- [42] C.E. Bamberger, G.M. Begun, H.W. Dunn, Journal of the American Ceramic Society 69 (1986) 93–94.
- [43] Z.F. Bian, J. Ren, J. Zhu, S.H. Wang, Y.F. Lu, H.X. Li, Applied Catalysis B: Environmental 89 (2009) 577–582.
- [44] J.C. Parker, R.W. Siegel, Applied Physics Letters 57 (1990) 943–945.
- [45] A.T. Bell, Science 299 (2003) 1688–1691.
- [46] S. Rengaraj, X.Z. Li, Chemosphere 66 (2007) 930–938.
- [47] A.Q. Jiang, Z.X. Hu, L.D. Zhang, Applied Physics Letters 74 (1999) 114.
- [48] L.D. Kong, H.H. Chen, W.M. Hua, S.C. Zhang, J.M. Chen, Chemical Communications 40 (2008) 4977–4979.
- [49] H. Hidaka, K. Ajisaka, S. Horikoshi, T. Oyama, K. Takeuchi, J. Zhao, N. Serpone, Journal of Photochemistry and Photobiology A: Chemistry 138 (2001) 185–192.
- [50] J.A. Byrne, B.R. Eggins, Journal of Electroanalytical Chemistry 457 (1998) 61–72.